

Escape patterns, magnetic footprints, and homoclinic tangles due to ergodic magnetic limiters

Elton C. da Silva and Iberê L. Caldas

Instituto de Física, Universidade de São Paulo, C.P. 66318, 05315-970 São Paulo, São Paulo, Brazil

Ricardo L. Viana

Departamento de Física, Universidade Federal do Paraná, C.P. 19081, 81531-990 Curitiba, Paraná, Brazil

Miguel A. F. Sanjuán

Nonlinear Dynamics and Chaos Group, Departamento de Ciencias Experimentales y Ingeniería, Universidad Rey Juan Carlos, Tulipán s/n, 28933 Móstoles, Madrid, Spain

(Received 26 June 2002; accepted 9 September 2002)

The action of a set of ergodic magnetic limiters in tokamaks is investigated from the Hamiltonian chaotic scattering point of view. Special attention is paid to the influence of invariant sets, such as stable and unstable manifolds, as well as the strange saddle, on the formation of the chaotic layer at the plasma edge. The nonuniform escape process associated to chaotic field lines is also analyzed. It is shown that the ergodic layer produced by the limiters has not only a fractal structure, but it possesses the even more restrictive Wada property. © 2002 American Institute of Physics. [DOI: 10.1063/1.1518681]

I. INTRODUCTION

One of the most important problems in a plasma-wall interaction in tokamaks is the control of plasma contamination due to localized heat and particle loadings on the inner tokamak wall.¹ It is believed that the impurity concentration in the plasma core could be reduced by a factor that is inversely proportional to the electron diffusion coefficient in the plasma edge.² Ergodic magnetic limiters (EML) have been proposed to uniformize these fluxes through the creation of chaotic magnetic field lines near the tokamak wall, which can be achieved by means of externally applied resonant fields.³

Although it is possible to use resonant helical windings to obtain an EML,⁴ a more practical design for it consists of using only slices of helical windings in the form of current rings.⁵ Experiments with EMLs^{6,7} have shown a decrease of the plasma temperature in the tokamak edge region and a reduction of the plasma-wall interactions, opening the possibility of controlling some magnetohydrodynamical (MHD) oscillation modes. Other experiments, however, in which a poloidal modulation of thermal fluxes has been observed,^{8,9} have put in doubt the claim that the chaotic boundary layer could uniformize heat and particle loadings on the tokamak wall.

Moreover, there is another and more fundamental problem yet to be completely solved, related to the particle anomalous diffusion in presence of chaotic magnetic field lines. Approaches based in classical and neoclassical transport theories have not been successful in explaining experimental data.^{10,11} The investigation of anomalous transport in the presence of chaotic magnetic field lines often needs the analysis of large bunches of magnetic field lines by a huge number of turns along the tokamak torus.¹² While the numerical integration of field line equations is, in principle,

always available, the use of field line mappings has proved to be very efficient and reliable.¹³

Thanks to magnetic flux conservation, a field line map must be area-preserving, such that the field line equations can be cast in a Hamiltonian form.¹⁴ Hamiltonian maps have been used to describe nonsymmetric perturbations in tokamaks due to ergodic divertors.^{15–19} The mapping approach has been first used in EML models in Ref. 5, where a map was derived by using a rectangular geometry appropriate to describe the immediate vicinity of the tokamak wall. Although this map has been improved in ensuing papers,^{20,21} it turns out that the use of simplified models may mask some important aspects of the physical setting, such as the role of toroidal effects and the Shafranov shift of magnetic surfaces.

A field line map has been recently proposed which embodies three important features: (i) a fully toroidal coordinate system; (ii) an equilibrium magnetic field obtained from an approximate analytical solution of the Grad-Schlüter-Shafranov equation; (iii) the design of the EML tries to follow the actual helical paths of field lines, taking into account pitch variations due to the toroidal geometry.^{22–24} This is a rigorously area-preserving map, and may be regarded as a canonical transformation between action-angle variables related to the geometrical field line coordinates.²¹ An explicit Hamiltonian function is obtained for the problem, assuming that the EML perturbation is a sequence of delta-function pulses.²⁵

We have used this map to study field line diffusion in the edge region of a tokamak with ergodic limiters.²³ Our results indicate that the process is initially superdiffusive due to the positiveness of the Lyapunov exponent, and subsequently reaches a plateau, after which there is a decay due to field line collisions with the tokamak wall. This field line loss has been described as an exponential-type decay following a Poisson distribution. Due to the existence of this wall this

$$q = q_c(r_t) \left(1 - 4 \frac{r_t^2}{R_0'^2} \right)^{-1/2}, \quad (5)$$

where

$$q_c(r_t) = \frac{I_e}{I_p} \frac{r_t^2}{R_0'^2} \left[1 - \left(1 - \frac{r_t^2}{a^2} \right)^{\gamma+1} \right]^{-1}. \quad (6)$$

In the following, we will choose $q \approx 1$ at the magnetic axis and $q \approx 5$ at the plasma edge ($r_t = a$), as a consequence of adopting $\gamma = 3$. We also normalize lengths to the minor radius ($b_t = 1$) and choose parameters so that $a/R_0' = 0.26$.^{10,37}

The magnetic structure of the plasma is studied by integrating the field line equations. Since the equilibrium magnetic field is axisymmetric, we may set the ignorable coordinate $\varphi_t = t$ as a time-like variable (to be used as a field line parametrization), and put the field line equations in a Hamiltonian form,^{14,38}

$$\frac{d\mathcal{I}}{dt} = - \frac{\partial H_0}{\partial \vartheta}, \quad \frac{d\vartheta}{dt} = \frac{\partial H_0}{\partial \mathcal{I}}, \quad (7)$$

where (\mathcal{I}, ϑ) are angle-action variables of the equilibrium Hamiltonian $H_0(\mathcal{I})$ given by

$$H_0(\mathcal{I}) = 2\pi \int \frac{d\mathcal{I}}{q(r_t(\mathcal{I}))}. \quad (8)$$

These angle-action variables are related to the toroidal polar coordinates in the following way:²²

$$\mathcal{I}(r_t) = \frac{1}{4} [1 - \Omega_+(r_t)\Omega_-(r_t)], \quad (9)$$

$$\vartheta(r_t, \theta_t) = 2 \arctan \left[\frac{\Omega_+(r_t)}{\Omega_-(r_t)} \tan \left(\frac{\theta_t}{2} \right) \right], \quad (10)$$

with

$$\Omega_{\pm}(r_t) = \sqrt{1 \pm 2 \frac{r_t}{R_0'}}. \quad (11)$$

The EML design which will be considered consists of one or more slices of a resonant helical winding with adequate mode numbers, located in suitable positions along the torus. The design of the corresponding helical winding needs to take into account the effects of the toroidal geometry, such that the helical pitch is not uniform due to the behavior of the toroidal field component, which is stronger in the inner part of the torus. We used a winding law to emulate the actual paths followed by magnetic field lines, introducing a tunable parameter λ , such that the variable $u_t = m_0(\theta_t + \lambda \sin \theta_t) - n_0\varphi_t$, where (m_0, n_0) are mode numbers, is constant along a given helical winding. The magnetic field generated by the corresponding helical winding has been obtained analytically by means of an approximate solution of the Laplace equation, supposing a vacuum field (valid for low-beta plasmas only). Proper boundary conditions are imposed, with the help of a singular current distribution, at the tokamak wall $r_t = b_t$.

The equilibrium Hamiltonian $H_0(\mathcal{I})$ is integrable, but the addition of a nonsymmetric perturbation caused by the EML rings (see Fig. 1) breaks the integrability of the system.

We model the action of N_r EML rings, equally spaced along the toroidal direction, on the equilibrium magnetic field lines as a sequence of pulses described by the following nonautonomous Hamiltonian:

$$H(\mathcal{I}, \vartheta, t) = H_0(\mathcal{I}) + \epsilon H_1(\mathcal{I}, \vartheta, t) \sum_{k=-\infty}^{\infty} \delta \left(t - k \frac{2\pi}{N_r} \right). \quad (12)$$

Since the perturbing Hamiltonian $H_1(\mathcal{I}, \vartheta, t)$ is periodic in ϑ and in $t = \varphi$, it can be written as

$$H_1(\mathcal{I}, \vartheta, t) = \sum_{m=0}^{2m_0} H_m^*(\mathcal{I}) e^{i(m\vartheta - n_0 t)}, \quad (13)$$

where the Fourier components $H_m^*(\mathcal{I})$ are²²

$$H_m^*(\mathcal{I}) = \sum_{m'=0}^{2m_0} H_{m'}(r_t(\mathcal{I})) \cdot S_{m,m'}(\mathcal{I}), \quad (14)$$

in which

$$H_{m'}(r_t) = -J_{m'-m_0}(m_0\lambda) \left(\frac{r_t}{b_t} \right)^{m'}, \quad (15)$$

$$S_{m,m'}(\mathcal{I}) = \frac{1}{2\pi} \int_0^{2\pi} e^{i[m'\theta_t(\mathcal{I}, \vartheta) - m\vartheta]} d\vartheta. \quad (16)$$

Due to the time dependence of the EML Hamiltonian in the form of a sequence of delta functions, it is possible to define discretized variables \mathcal{I}_n and ϑ_n as the corresponding values of the action-angle variables just after the n -th crossing of a field line with the plane $\varphi_k = t_k = 2\pi k/N_a$, with $k = 0, 1, 2, \dots, N_a - 1$.²⁰ In the field line equations, the action-angle variables are continuous through the delta functions at times $t_k = k(2\pi/N_a)$, $k = 0, \pm 1, \pm 2, \dots$, but their derivatives are not; such that we evaluate the corresponding jumps due to the delta functions. Proceeding in this fashion we can obtain the following area-preserving mapping:²²

$$\mathcal{I}_{n+1} = \mathcal{I}_n + \epsilon f(\mathcal{I}_{n+1}, \vartheta_n, t_n), \quad (17)$$

$$\vartheta_{n+1} = \vartheta_n + \frac{2\pi}{N_r q(\mathcal{I}_{n+1})} + \epsilon g(\mathcal{I}_{n+1}, \vartheta_n, t_n), \quad (18)$$

$$t_{n+1} = t_n + \frac{2\pi}{N_r}, \quad (19)$$

where

$$f = - \frac{\partial H_1}{\partial \vartheta}, \quad g = \frac{\partial H_1}{\partial \mathcal{I}}, \quad \text{and} \quad \epsilon = 2 \frac{I_h l}{I_e R_0'}. \quad (20)$$

It should be remarked, however, that there are other possible ways to derive a symplectic map from a Hamiltonian system, like the method described in Ref. 39.

In Fig. 2, we show a Poincaré section of many orbits obtained from the above mapping. In order to assure a good accuracy for the numerical chaotic orbits we have iterated the map equations using extended precision. We use $N_r = 4$ rings, a perturbation strength of $\epsilon = 1.17 \times 10^{-4}$, EML helical excitation modes $(m_0, n_0) = (5, 1)$ and a current modulation

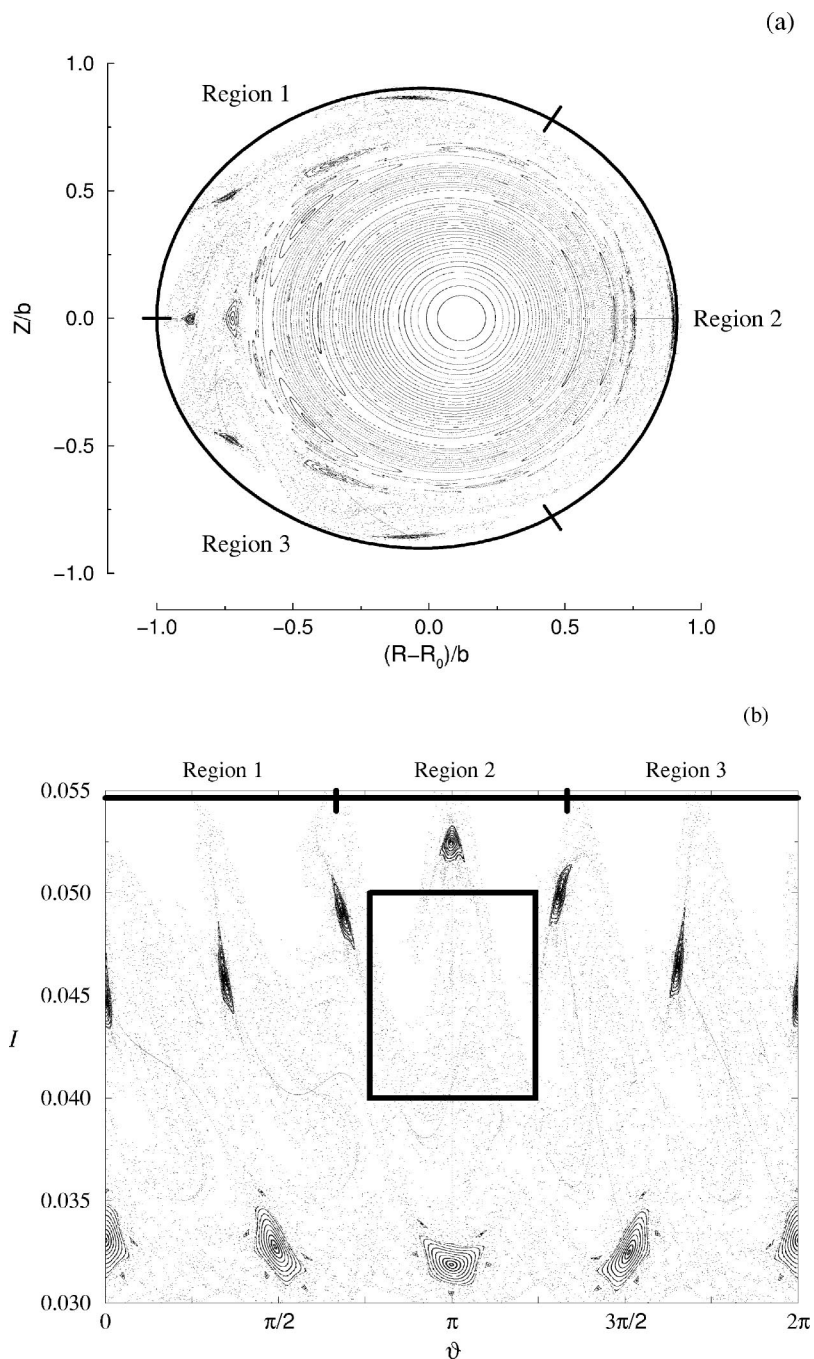


FIG. 2. Poincaré cross-section for the EML map: (a) in terms of the usual polar coordinates; (b) a close-up view of the plasma edge in terms of angle-action variables.

parameter $\lambda = 0.53$, compatible with the chosen EML mode numbers. We choose these numerical values having in mind a limiter design and parameters taken from the tokamak TCABR,⁴⁰ and for the equilibrium conditions described in Sec. II [$a/R_0' = 0.26$ and $q(a) \approx 5.0$], and a limiter current of the order of 5% of the plasma current ($I_P = 70$ kA). The latter value is typical for ergodic limiters but slightly higher than those used in ergodic divertors, inasmuch as the perturbation caused by an ergodic limiter (EML) is more localized in space than for an ergodic divertor.^{15–19}

Figures 2(a) and 2(b) depict the Poincaré sections in polar and action-angle variables, respectively; the latter being more convenient to highlight the physics at the tokamak edge. The general features displayed by Fig. 2 are fairly

well-known, since one has a divided phase space comprising of (i) resonances, characterized by periodic islands with a pendular shape, which appear due to the breaking of equilibrium flux surfaces with rational safety factors. They correspond to Poincaré–Birkhoff periodic orbits of the EML map; (ii) KAM tori, corresponding to surviving, yet deformed flux surfaces for which the safety factor is irrational; (iii) chaotic area-filling orbits, which appear due to the homoclinic and/or heteroclinic crossings of the invariant manifolds of unstable Poincaré–Birkhoff periodic orbits.⁴¹ Locally chaotic orbits at the resonance borders may fuse, as the perturbation strength builds up, and a globally chaotic region merges as a consequence.

The EML action requires this globally chaotic region to

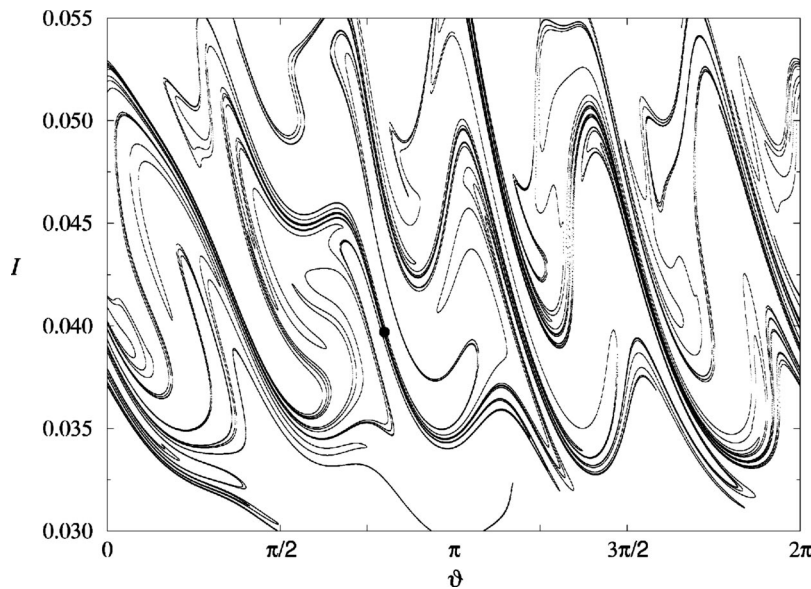


FIG. 3. Unstable manifold of the unstable period-5 orbit (shown as a bullet).

extend from the outer plasma portion to the tokamak inner wall. This chaotic region is far from being uniform, however, for it presents densely intertwined regions: one from where the field lines hit the tokamak wall with relatively short connection length (white areas in Fig. 2); and another one where the area-filling field lines take a large number of turns before eventually hit the tokamak wall. Both regions have periodic islands of stability embedded in them, in such a way that a set of initial conditions with a positive Lebesgue measure generates nonchaotic field lines. These orbits do not play a significant role in the forthcoming discussions.

III. INVARIANT SETS FOR THE EML MAP

Dissipative dynamical systems typically present invariant sets named attractors, to which asymptote orbits originated from a set of initial conditions called its basin of attraction. Nonattracting chaotic invariant sets, on the other hand, have equally important dynamical consequences, and are responsible for phenomena like fractal basin boundaries,⁴² transient chaos,⁴³ crises and chaotic scattering.²⁷ This is particularly important in Hamiltonian, or area-preserving systems, where there are no attractors.

Consider an unstable periodic orbit embedded in the chaotic region depicted in Fig. 2. Due to the area-preserving nature of the EML map it will be a saddle orbit, with one stable and one unstable direction. The stable (unstable) manifold at this point is the set of points which asymptote to the periodic orbit under the forward (backward) iterations of the map, as time goes to infinity. The sets are invariant in the sense that the map iterations of points belonging to these manifolds remain in them for all times. A strange saddle is a nonattracting chaotic invariant set formed by the intersection of the stable and unstable manifolds of unstable saddle points, and also contains a dense orbit. The stable and unstable manifolds intersect transversally at homoclinic or heteroclinic points, and these points map one another, such that there is an infinite number of unstable points embedded in the chaotic saddle, with Lebesgue measure zero.²⁸

Let $\mathbf{T}(\mathbf{x})$ represent the two-dimensional EML map (17), where $\mathbf{x} \equiv (I, \vartheta)$. We obtain the stable and unstable manifolds for an unstable periodic orbit embedded in the chaotic region by using the following procedure.⁴⁴ First, we choose a period- k unstable saddle orbit \mathbf{x}^* , i.e., a solution of the equation $\mathbf{T}^k(\mathbf{x}^*) = \mathbf{x}^*$. We linearize the map at the point \mathbf{x}^* and evaluate the corresponding eigenvalues and eigenvectors. Since \mathbf{x}^* is a hyperbolic saddle, the eigenvalues are real and have moduli greater than and less than unity, and are related to invariant unstable and stable subspaces, respectively. These subspaces, on the other hand, are tangent to the unstable and stable manifolds at \mathbf{x}^* .

Then we find a point \mathbf{x}_a along the unstable subspace such that $\mathbf{x}_b = \mathbf{T}^k(\mathbf{x}_a)$ is less than a small factor (say, 10^{-6}) apart from \mathbf{x}^* . The points \mathbf{x}_a and \mathbf{x}_b define a line segment γ_u , from which we generate a set of partition points $\{\gamma_{u_i}\}_{i=1}^M$. The unstable manifold is the closure of the set of successive images of $\{\gamma_{u_i}\}_{i=1}^M$ under the k -times iterated map $\mathbf{T}^k(\mathbf{x})$. Likewise, the stable manifold is the union of the set of successive preimages of $\{\gamma_s\}_{i=1}^M$ under the mapping $\mathbf{T}^{-k}(\mathbf{x})$. In Figs. 3 and 4, for which the parameters were chosen to match those of Fig. 2, we show the unstable and stable manifolds, respectively, of a period $k=5$ hyperbolic fixed point indicated as a filled circle.

The chaotic saddle is the intersection of Figs. 3 and 4, and is a Lebesgue measure zero set of points. Points exactly on the chaotic saddle are bound to remain there for all forward and backward iterations of the map. If a field line starts off but near the chaotic saddle, it will wander along the tapestry of unstable orbits in an erratic way, approaching arbitrarily close any unstable orbit embedded in the chaotic saddle. This makes for a chaotic orbit in the layer produced by the EML, and Figs. 3 and 4 show the extremely convoluted structure of the invariant manifolds, with the characteristic stretching–folding behavior.

Another numerical technique to obtain approximations of the invariant manifolds and the associated chaotic saddle is the *sprinkler method*.^{45,46} We partition the phase portrait in

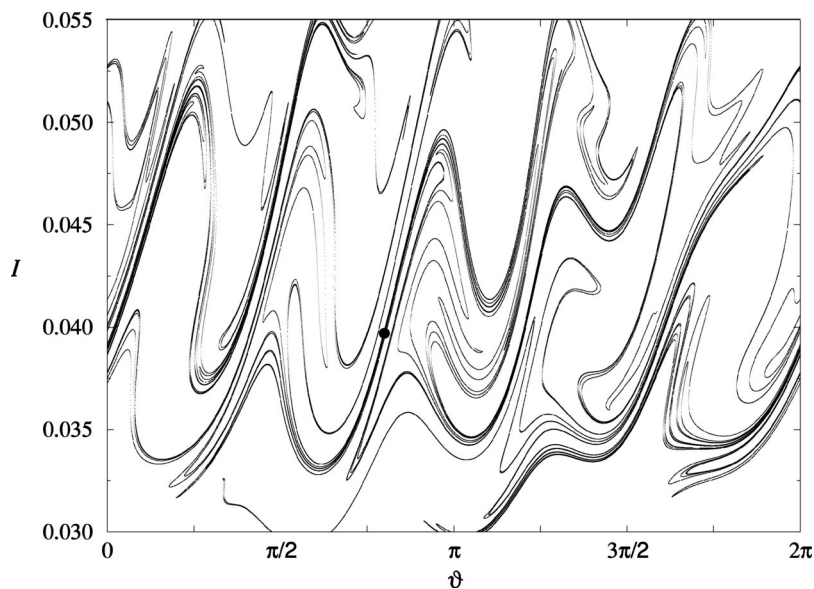


FIG. 4. Stable manifold of the unstable period-5 orbit (shown as a bullet).

the chaotic region of interest (near the tokamak wall) into a fine grid of points, and iterate each grid point n times. Once the resulting field line trajectory reaches the wall for finite n it is considered lost and the further iterates are not plotted. We pass to the next grid point and so on. For sufficiently large n and a grid fine enough, trajectories that do not hit the wall in n iterates can be used to generate an approximation to the unstable manifold. The chaotic saddle itself can be approximated by half (or some other fraction) of the iterates $n' = \chi n$, with $0 < \chi < 1$. Now repeat the process for the backward iterates, i.e., iterate each grid point a large number of negative times, retaining only the grid points generating trajectories that do not hit the wall after n backward iterates. These points approximate the stable manifold of the chaotic saddle. We have used this method to obtain the unstable and stable manifolds for the EML map, and the results are entirely similar to the previous method. For a yet more sophisticated approach, there is the PIM-triple method,⁴⁷ but it would not give results appreciably better than those presented in Figs. 3 and 4.

We close this section by mentioning that the invariant manifold structure here described shall be used throughout this paper to explain the fractal nature of the deposition patterns on the tokamak wall, namely the exit basins and the magnetic footprints, to be discussed in the next two sections.

IV. EXIT BASINS FOR THE EML MAP

Suppose we choose at random a magnetic field line with initial condition located outside the last closed magnetic surface, i.e., in the chaotic region near the tokamak wall. We can think of it as a trajectory that eventually goes to the tokamak wall by iterating the mapping forward to $n \rightarrow \infty$. This occurs because the wall at $r_i = b_i$ is actually an arbitrary partition in the phase portraits, and the chaotic region intersects the line $r_i = b_i$ at a segment of a finite Lebesgue measure. In terms of the analogy with chaotic scattering process, we may consider these field lines as *outgoing* trajectories. Since the EML map is invertible, the same initial conditions

generate field lines that eventually hit the wall as $n \rightarrow -\infty$ when we iterate the map backwards. Accordingly, we consider them as *ingoing* trajectories.

Although this scenario is actually very similar to the one present in chaotic scattering process in open Hamiltonian systems, there are some important differences. First, the entire picture is static, since time here is just a convenient parametrization of field lines. Second, in a conventional chaotic scattering process, the ingoing and outgoing regions are usually different, but in the EML case they are the actually same physical region, namely the tokamak wall. Apart from these differences, this analogy can be pushed forward in all mathematical aspects.

While for dissipative systems we speak of basins of attraction to refer to the set of initial conditions which converge to a given attractor, it is possible to extend this concept for including the set of initial conditions which generates trajectories that escape through a given exit, in an open Hamiltonian system.^{27,48} This set is called an *exit basin*. When there are two (or more) exits in the system one is interested in the exit basin boundary, which can be either smooth or fractal, as for basins of attraction of dissipative systems. Fractal boundaries are important dynamical objects because orbits that start in their vicinity exhibit very complicated and unpredictable motion.

Examples of exit basins have been given in the literature for the Sinai billiard with two holes,²⁷ scattering by three circular disks and by a Hénon–Heiles potential.³² The above-mentioned analogy with chaotic scattering makes it natural to extend the exit basin concept to the chaotic region existent for the EML map (17). In this case, we divide the tokamak wall into three poloidal sections of equal length, $0 \leq \vartheta < 2\pi/3$, $2\pi/3 \leq \vartheta < 4\pi/3$, and $4\pi/3 \leq \vartheta < 2\pi$, indicated, respectively as regions 1, 2, and 3 in Fig. 2, corresponding to different exits for a chaotic field line.

In order to obtain the exit basins we used a fine grid of 600×700 points chosen inside the small rectangle shown in Fig. 2(b), and which comprises a representative part of the

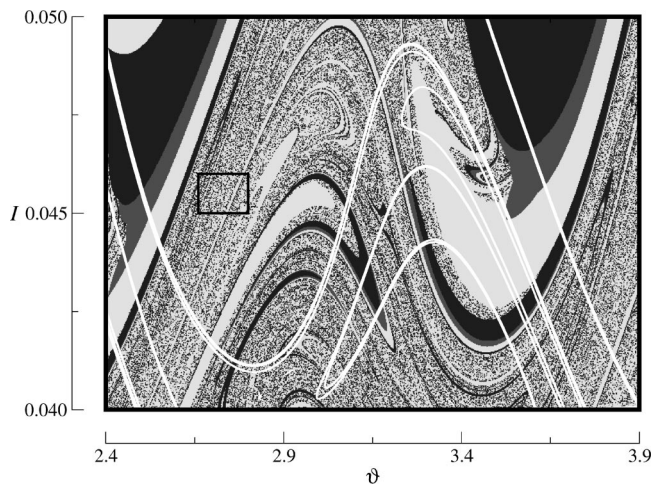


FIG. 5. Exit basin for the EML map. The regions in dark gray, light gray, and black correspond to field lines colliding with the tokamak wall at the regions marked 1, 2, and 3, respectively, in Fig. 2. We also show (solid white line) a segment of the unstable manifold of a fixed point embedded in the chaotic region.

chaotic region near the wall. We mark the initial condition pixel in dark gray, light gray, or black, depending on whether the field line goes to the wall section called region 1, 2, or 3, respectively, under the forward dynamic. Figure 5 shows that the three exit basins are intertwined in a very complex way, with many similarities with basins of attraction of systems like forced pendula.⁴⁹ In particular, we argue that the exit basin boundary in Fig. 5 is fractal.

Before checking the latter statement, it is useful to compare Fig. 5 with the same region of Fig. 4, what illustrates the known fact that the basin boundary coincides with the stable manifold of the chaotic saddle. In fact, the boundary is the closure of the stable manifold of a saddle periodic orbit.⁴² The convoluted shape of the boundary suggests that it has a smooth component (along the stable manifold) and a fractal one, transversal to it, and akin to a Cantor set. This is best evidenced by magnifying Fig. 4, and the sequence of blow-ups shown in Figs. 6 and 7 strongly suggests a self-similarity in the basin striations, a characteristic of fractal curves in the plane.⁴⁹

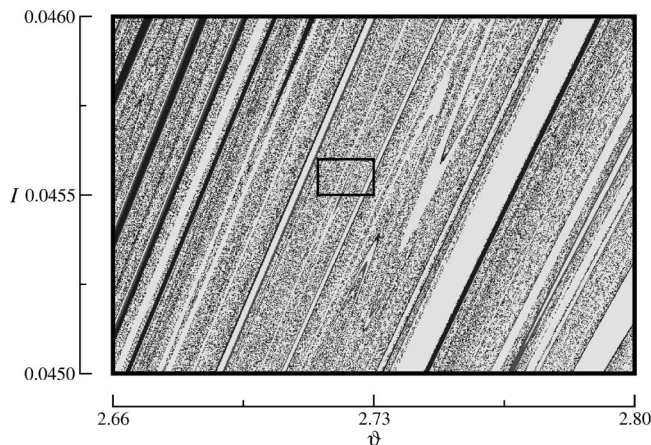


FIG. 6. Blow-up of the rectangle marked in Fig. 5.

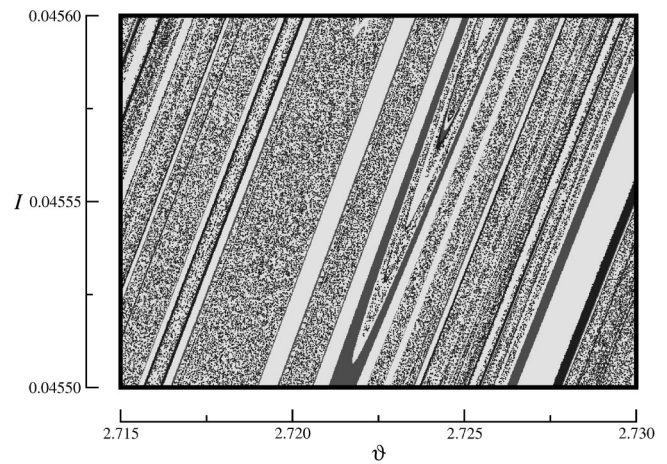


FIG. 7. Blow-up of the rectangle marked in Fig. 6.

We calculate the uncertainty dimension for the exit basin boundary of Fig. 4, by using the algorithm extensively used for basins of attraction.⁴² Instead of covering the region containing the exit boundary with a fine and regular mesh of points we randomly choose initial conditions $(\mathcal{I}_0, \vartheta_0)$ in this region and iterate forward the EML map until the corresponding field lines hit the wall. Then, we iterate forward the field lines with slightly displaced initial conditions $(\mathcal{I}_0 + \epsilon, \vartheta_0)$ and $(\mathcal{I}_0 - \epsilon, \vartheta_0)$, for a small ϵ , also until they collide with the wall. If both displaced initial conditions go to the same region of the wall that the field line with initial condition $(\mathcal{I}_0, \vartheta_0)$ has gone to, then this initial condition is *certain*. Otherwise, it will be dubbed *uncertain*.

This procedure is repeated for a large number of initial conditions N_T , of which N_u are uncertain, what gives an estimate of the fraction of uncertain initial conditions $f(\epsilon) \approx N_u/N_T$. Considering different values of ϵ , we expect that this uncertain fraction scales with ϵ as a power law $f(\epsilon) \sim \epsilon^\alpha$, where α is the uncertainty exponent of the exit basin boundary. Smooth basin boundaries scale linearly with ϵ , i.e., $\alpha = 1$, for the uncertain fraction would be simply a strip of width 2ϵ stranding the basin boundary. Fractal basin boundaries, on the contrary, have a worse scaling, in that we expect $0 < \alpha < 1$, i.e., a given improvement in the accuracy used in the initial condition determination does not imply a substantial reduction of the uncertain fraction. This has been called *final-state sensitivity*, and it turns to be an obstacle to predictability in dynamical systems even when they are not chaotic.⁴³

Figure 8 depicts the uncertain fraction $f(\epsilon)$ vs ϵ for more than three decades of variation. The solid line is a least squares fit that confirms the power-law scaling characteristic of fractal boundaries, with uncertainty exponent $\alpha = 0.0763 \pm 0.0006$ for the forward iterations, and $\alpha = 0.0761 \pm 0.0007$ for the backward iterations. The extreme convoluted nature of the exit basins apparent in Fig. 5 is reflected in the very small value obtained for α .

Let D_0 be the box-counting (or capacity) dimension of the exit basin boundary. It can be proved that $\alpha = D - D_0$, where $D = 2$ is the phase space dimension.⁴² Since the basin boundary is the closure of the stable manifold of the chaotic

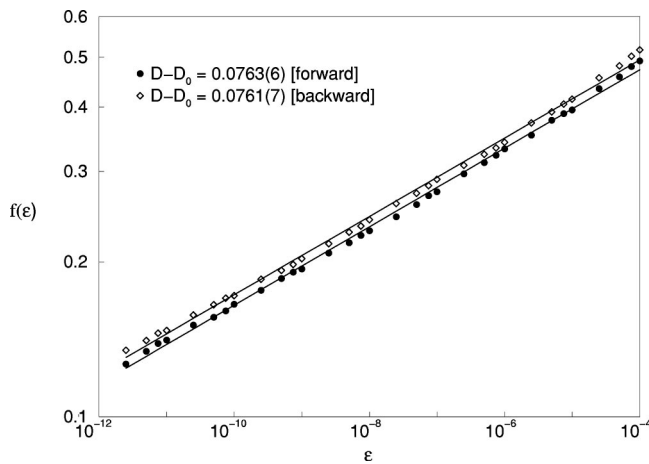


FIG. 8. Uncertain fraction for initial conditions randomly chosen in the chaotic region depicted in Fig. 2. We show least squares fits obtained for forward (bullets) and backward (diamonds) iterations of the EML map.

saddle, the basin boundary dimension is equal to the stable manifold dimension $D_0 = D_s$. Furthermore, since the map is area-preserving, the dimension of the unstable and stable manifolds are the same: $D_u = D_s$. We have computed the box-counting dimensions of the invariant manifolds (see Fig. 8), and found that $D_s = 1.9237 \pm 0.0006$ and $D_u = 1.9239 \pm 0.0007$. Since the chaotic saddle is the intersection of the stable and unstable manifolds, its dimension is given by

$$D_{cs} = D_s + D_u - D = 2(D_0 - 1) = 2(D - \alpha - 1). \quad (21)$$

Considering the above values for D_s and D_u we have $D_{cs} = 1.8476 \pm 0.0009$, which is close to the dimension of the phase space itself.

The convoluted nature of the exit basins can be understood as a consequence of the chaotic saddle underlying the dynamics in the chaotic layer near the wall. Let us consider a given partitioning line in the tokamak wall dividing two adjacent regions (1, 2, or 3). Because of the uniqueness property of the differential field line equations we have that the chaotic scattering region is also divided in two (or more) parts, which are the exit basins. If the partitioning line crosses the stable or unstable manifold of the chaotic saddle, the exit basin boundary is fractal. The key point is that a finite segment of the partitioning line is smoothly deformed before reaching the chaotic saddle. Points lying on its stable and unstable manifolds remain attached to the chaotic saddle for any time. On the other hand, the segments of the partitioning line in between the manifolds become increasingly elongated and converge to the manifold.⁵⁰

In order to illustrate this process, in Fig. 9 we show schematically one unstable fixed point belonging to the chaotic saddle and its corresponding manifolds. The image of the partitioning line under the forward iterations of the EML map is supposed to cross the stable manifold. The forward images of this boundary approach the fixed point such that (i) the intersection points between the stable manifold and the boundary converge exponentially fast according to the corresponding eigenvalue of the map linearized at the fixed point (with modulus less than unity); (ii) the length of the lobes increase exponentially in order to preserve areas, and

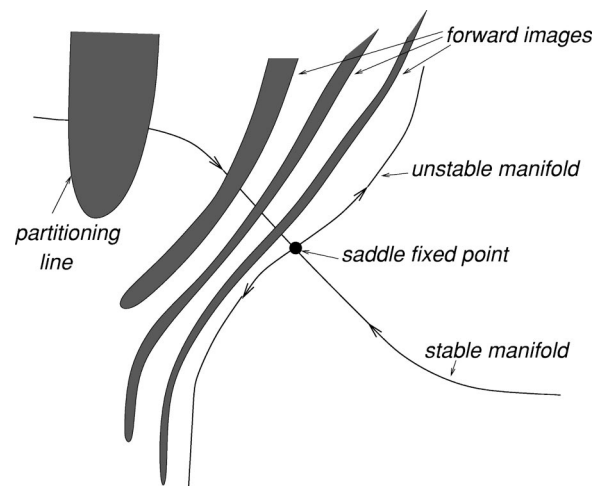


FIG. 9. Schematic picture of the accumulation of exit basin filaments at the unstable manifold of a saddle point.

the lobes tend to follow the unstable manifold.⁵⁰ The union of all images of the boundary forms a curve that oscillates wildly as it approaches the unstable fixed point. The net effect is that segments of the partitioning line will accumulate on the filaments of the unstable manifold.

The same is true for the backward images of the partitioning line. Segments of it lying between the filaments of the unstable manifold will be transported due to the backward dynamics to the scattering region, and they will accumulate asymptotically on the filaments of the stable manifold. Thus, the boundary of the exit basins contains the stable and unstable manifolds of the chaotic saddle, or at least a part of them. It should be remarked that it is necessary that the exit boundary intersects the manifold so as to have a fractal component. The lobes approaching the fixed point smoothly extend along some manifold, so representing the smooth (nonfractal) component of the exit boundary. On the other hand, we claim that the fractal component of the exit basin boundary is responsible for the nonuniformity of the heat and particle loadings on the tokamak wall.

V. ESCAPE PATTERNS AND MAGNETIC FOOTPRINTS

One of the main consequences of nonattracting chaotic sets in a chaotic scattering problem is that an orbit may spend a long time in the vicinity of the chaotic saddle before escaping. Usually, for nonattracting chaotic systems, the number of orbits that remain in the scattering region after a time n decreases exponentially. In fact, the system typically spends a transient time n_0 before any orbit escapes. So the number of orbits that remain after a time n is

$$\mathcal{N}(n) = \mathcal{N}_0 e^{-(n-n_0)/\tau}, \quad (22)$$

where \mathcal{N}_0 is the total number of initial orbits and $(1/\tau)$ is the exponential decay rate.

We have already reported this property for the EML map in a previous work dealing with the number of field lines lost due to collisions with the wall.²³ The escape plot of Fig. 10 depicts in grayscale the number of toroidal turns (*escape times*) it takes for a field line to reach the tokamak wall. The

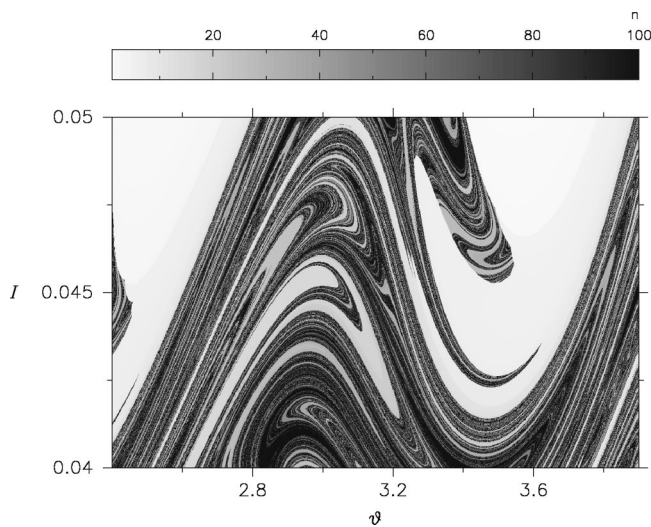


FIG. 10. Escape time (measured in number of toroidal turns) for initial conditions randomly chosen in Fig. 2. The darker is the pixel the larger is the corresponding time it takes to the field line to reach the wall.

resulting figure is very similar to the exit basin structure shown in Fig. 5. In particular, those regions from where the field lines rapidly escape coincide with regions where the boundaries are smooth. This similarity indicates that the escape plot and the exit basin plot might have the same fractal properties, even though, in this situation, we have many more basins involved. In fact, we have in Fig. 10 an infinite number of basins, each one linked to a specific *escape time*.

In order to explore this similarity in more depth, let us consider a field line connecting two points on the wall. This field line enters into the chaotic region and, after some erratic turns around the torus it returns back to the wall. Figure 11 shows the dependence of the escape time on the initial poloidal angle (ϑ_i) for a fixed value of \mathcal{I} corresponding to the wall position. The number of toroidal turns it takes for a field line to return back to the wall as a function of the initial poloidal angle shows sharp peaks with a Cantor-like struc-

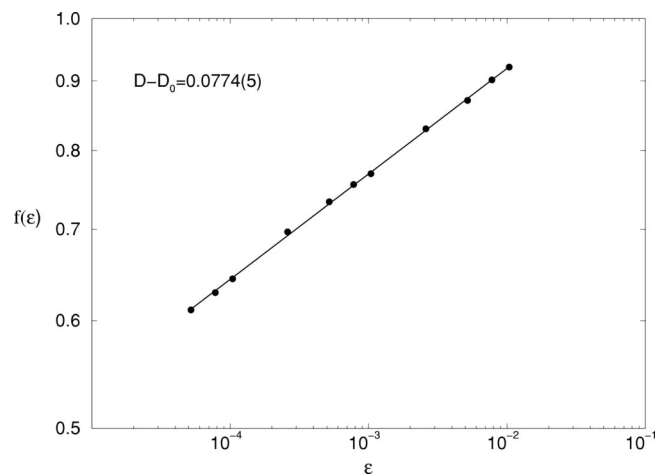


FIG. 12. Uncertain fraction for initial conditions randomly chosen in Fig. 11. The solid line corresponds to a least squares fit.

ture. This results from the intersection of the stable manifold, which we have shown to have a fractal transverse component, and the smooth line of initial poloidal angles. In order to verify that, we compute the box-counting dimension of the peaked curve in Fig. 11, through the uncertainty dimension method described in the previous section.

We choose at random a field line with initial poloidal angle ϑ_i on the wall, and two other field lines with angles $\vartheta_i - \epsilon$ and $\vartheta_i + \epsilon$. We determine the number of turns each field line takes to return back to the wall. If these numbers of turns are equal we label the angle ϑ_i as ϵ -certain, and uncertain otherwise. The uncertain fraction of initial poloidal angles is expected to scale with ϵ in a power-law fashion, with uncertainty exponent $\tilde{\alpha} = D_L - D_F$, where $D_L = 1$ is the dimension of the line of initial poloidal angles and D_F is the box-counting dimension of the Cantor-like set shown in the peaked curve in Fig. 11. In Fig. 12, we show $f(\epsilon)$ as a function of ϵ , from which the uncertainty exponent is $\alpha = 0.0774 \pm 0.0005$, and the corresponding box-counting di-

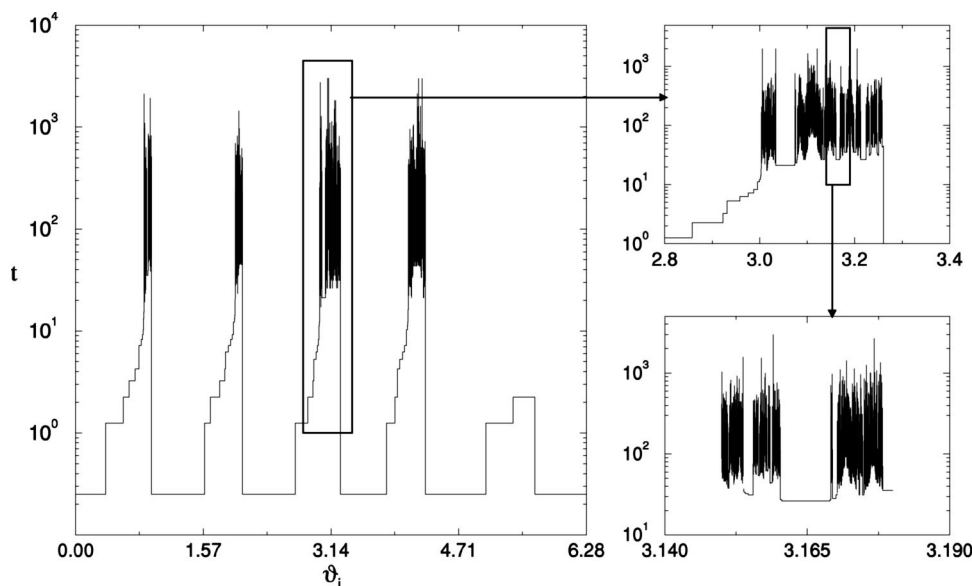


FIG. 11. Escape time versus initial poloidal angle, ϑ_i , for the situation depicted in Fig. 10. Two magnifications of the fractal peak structure are shown.

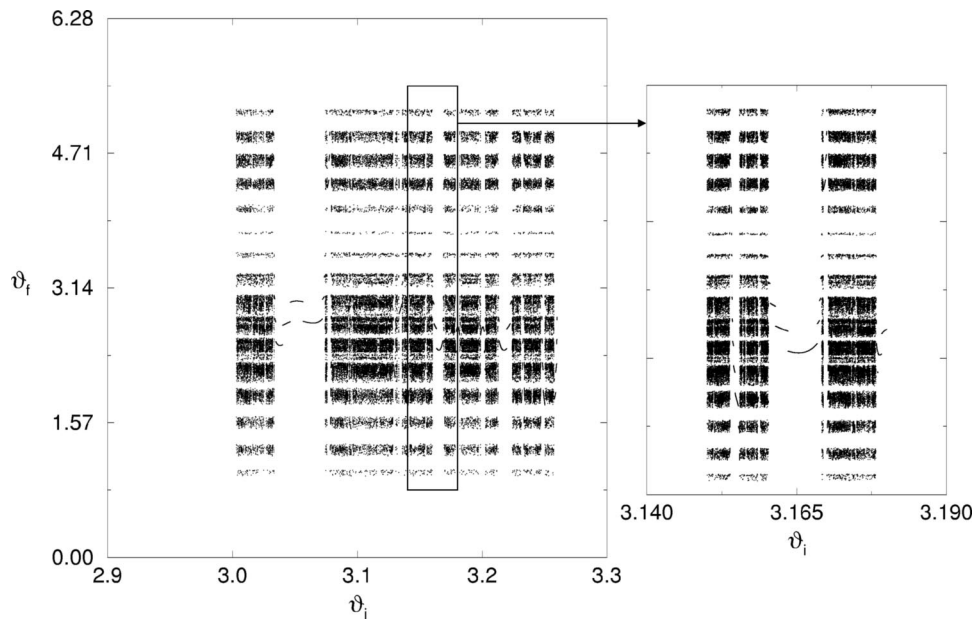


FIG. 13. Field line final poloidal angle (at the tokamak wall) versus initial poloidal angle for the situation depicted in Fig. 10. A magnification of the fractal structure is shown.

mension for the fractal curve is $D_F = 0.9226 \pm 0.0005$. Since this fractal curve is the intersection between the stable manifold and the one-dimensional line of initial poloidal angles, its box-counting dimension is given by $D_F = D_s + D_L - D$, hence $D_s = D_F + D - D_L = 1.9226 \pm 0.0005$, is in a good agreement with the result obtained in Sec. IV.

Field lines which take a long time to escape play an important role for heat and particle deposition on the tokamak wall. Such field lines come from the core of the chaotic region and can thus bring energetic plasma particles to the wall. These field lines enter into the chaotic region coming from a Cantor-like set of initial poloidal angles on the wall and they return back to the wall in a Cantor-like set of final poloidal angles as well. Therefore, we expect that the heat and particle deposition patterns also present a Cantor-like structure if the cross-field diffusion of particles does not fuzzy them so much. Those deposition patterns are usually known as *magnetic footprints*, characterized by very irregular stripped patterns. On the other hand, field lines corresponding to windows of constant escape time in Fig. 11 produce regular deposition patterns when they reach the wall. This is shown by Fig. 13, where we depict the final poloidal angle ϑ_f (when a field line has collided with the wall) as a function of the initial poloidal angle, ϑ_i , for initial conditions chosen inside a magnified box taken from Fig. 11.

VI. WADA PROPERTY OF THE EXIT BASINS

Consider an exit basin \mathcal{B} , like those represented in Fig. 5. A point p is a boundary point of the basin \mathcal{B} if every open neighborhood of p intersects the basin \mathcal{B} and at least another basin. The basin boundary is the set of all boundary points of that basin. Furthermore, the boundary point p is also a *Wada point* if every open neighborhood of p intersects at least three different basins. A basin boundary is said to possess the *Wada property* if every boundary point of \mathcal{B} is a Wada point, such that the boundary of such a basin is a *Wada basin*

boundary.⁴⁵ When two or more exit basins in a given system, it may well happen that these basins present the Wada property.^{52,53}

A strong condition that indicates if a basin boundary has the Wada property is that the unstable manifold of an unstable periodic point p must intersect every basin. This condition is necessary, but not sufficient. *At least one* of the complementary conditions listed below has to be satisfied:⁵¹

(i) The stable manifold of the saddle point p must be dense in the boundary of the three regions; (ii) the periodic orbit p must be the only accessible orbit from the basin \mathcal{B} . Otherwise, every unstable manifold of other periodic orbits that are accessible from \mathcal{B} must intersect all basins; (iii) the periodic orbit p must generate a basin cell.

The direct numerical verification of these complementary conditions is rather difficult, so that we used another way of showing the Wada property for the exit basins of the EML map,⁴⁸ and which consists on checking that every open neighborhood of a boundary point intersects at least three different basins. Let us take a point p on the exit boundary for the EML map, which actually coincides with the stable manifold of some periodic point which contains the point p . Around this point we take a small droplet \mathcal{D} of radius ϵ , and obtain its i -th forward image $\mathcal{D}_i = \mathbf{T}^i(\mathcal{D})$ under the map (40). When $i \rightarrow \infty$ this image is a convoluted and very thin ribbon extending along the unstable manifold. The droplet is a connected set, thus its images under $\mathbf{T}(\mathbf{x})$ are similarly connected. Consider now that there is a finite number m such that \mathcal{D}_m intersects all the exit basins. Because \mathcal{D}_m maps to \mathcal{D} under the m backward iterations, all the basin structures present in \mathcal{D}_m are mapped into \mathcal{D} . Since we did not make any particular assumption about the radius of the droplet, and the point p can be anywhere on the stable manifold, this statement is valid for any ϵ , such that the entire stable manifold is a Wada basin boundary.

The forward dynamics of a droplet is illustrated in Fig. 14. Observe how the image of the droplet looks like the

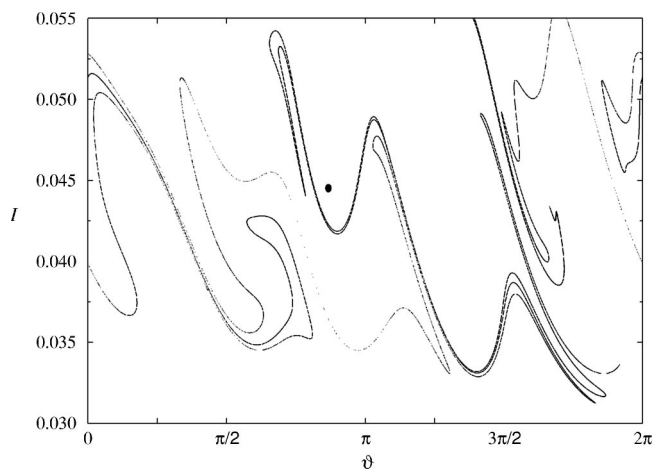


FIG. 14. The forward image of a small droplet (identified as a bullet) after 20 iterations of the EML map, for the same parameters as in Fig. 2.

unstable manifold of an unstable periodic orbit embedded in the chaotic region, as schematically illustrated by Fig. 7 (see also Fig. 3). Since the unstable manifold crosses all exit basins, as indicated in Fig. 5 by a white line, a droplet of any size will have intersections with all exit basins. On the basis of the above reasoning, we say that the exit basins shown have the Wada property, and possess a yet more complicated structure than ordinary fractal objects, which partially explains the very small values found for the uncertainty exponent.

We point out possible practical consequences of the Wada property: the deposition patterns on the tokamak wall may reveal a complicated mixing between footprints of hot and cold particles of the plasma. This can be of interest, for example, if the plasma is subjected to a noninductive current drive by beam injection.

VII. CONCLUSIONS

We have studied the action of a set of ergodic magnetic limiters (EML) from the point of view of Hamiltonian chaotic scattering processes in open systems. We have paid special attention to the structure of exit basins and its relation with invariant sets such as stable and unstable manifolds and chaotic saddles. In particular, the exit basin boundaries are given by the stable manifolds of periodic points embedded in the chaotic layer near the tokamak wall. We have computed the fractal dimensions of some relevant invariant sets and the exit basin boundaries.

The escape pattern of chaotic magnetic field lines gives us an accurate picture of the process whereby field lines are lost due to collisions with the tokamak wall. It was studied by means of escape plots, which presented the same fractal structure as the exit basins themselves. This was noticed analyzing how large field lines connecting wall to wall are. Those field lines, which spend a large number of toroidal turns before hitting back the wall, come from a Cantor-like set of initial poloidal angles on the wall. This Cantor-like set is the intersection of the stable manifold and a curve of initial poloidal angles. The set of final poloidal angles, connecting wall to wall through field lines coming from deep chaotic

regions, forms a stripped-like structure on the tokamak wall called a magnetic footprint, with the same Cantor-like structure as the set of initial poloidal angles for long chaotic field lines. We have observed even the more restrictive Wada property for exit basins, which puts into evidence the phenomenon of final-state sensitivity, extensively investigated for dissipative systems.

In our study we aimed to clarify the mechanism leading to the experimentally observed nonuniformity of the plasma-wall interactions due to the formation of the chaotic layer by an EML. The homoclinic tangle formed by stable and unstable manifolds of unstable periodic orbits embedded in the chaotic layer creates channels through which the field line escape is considerably faster. The resulting fractal structure of the magnetic footprints suggest that, according to the experimental findings, the heat and particle loadings on the tokamak wall are not uniform. Another physical consequence is the non-Gaussian nature of the diffusive process, leading to superdiffusive transport influenced by the escape channels.

ACKNOWLEDGMENTS

The authors are grateful to Professor Celso Grebogi for useful discussions and comments.

This work was made possible through partial financial support from the following Brazilian research agencies: FAPESP (São Paulo), CNPq, Fundação Araucária (Paraná), and FUNPAR (UFPR). M.A.F.S. acknowledges financial support by the Spanish Ministry of Science and Technology under Project No. BFM 2000-0967.

- ¹W. Engelhardt and W. Feneberg, *J. Nucl. Mater.* **76/77**, 518 (1978).
- ²W. Feneberg, *Proceedings of the 8th European Conference on Controlled Fusion and Plasma Physics* (European Physical Society, Petit-Lancy, 1977), Vol. 1, p. 3.
- ³F. Karger and K. Lackner, *Phys. Lett. A* **61**, 385 (1977).
- ⁴W. Feneberg and G. H. Wolf, *Nucl. Fusion* **27**, 669 (1981).
- ⁵T. J. Martin and J. B. Taylor, *Plasma Phys. Controlled Fusion* **26**, 321 (1984).
- ⁶N. Ohya, J. S. deGrassie, N. H. Brooks *et al.*, *J. Nucl. Mater.* **121**, 363 (1984).
- ⁷M. S. T. Araújo, A. Vannucci, and I. L. Caldas, *Nuovo Cimento D* **18**, 807 (1996).
- ⁸S. Takamura, Y. Shen, H. Yamada *et al.*, *J. Nucl. Mater.* **162–164**, 643 (1989).
- ⁹Y. Shen, M. Miyake, S. Takamura *et al.*, *J. Nucl. Mater.* **168**, 295 (1989).
- ¹⁰A. J. Wooton, B. A. Carreras, H. Matsumoto, K. McGuire, W. A. Peebles, Ch. P. Ritz, P. W. Terry, and S. J. Sweben, *Phys. Fluids B* **2**, 2879 (1990).
- ¹¹F. Wagner and U. Stroth, *Plasma Phys. Controlled Fusion* **35**, 1321 (1993).
- ¹²D. F. Duchs, A. Montvai, and C. Sack, *Plasma Phys. Controlled Fusion* **33**, 919 (1991).
- ¹³R. Balescu, M. Vlad, and F. Sineanu, *Phys. Rev. E* **58**, 951 (1998).
- ¹⁴P. J. Morrison, *Rev. Mod. Phys.* **70**, 467 (1998).
- ¹⁵Ph. Ghendrih, A. Grosman, and H. Capes, *Plasma Phys. Controlled Fusion* **38**, 1653 (1996).
- ¹⁶S. S. Abdullaev, K. H. Finken, A. Kaleck, and K. H. Spatschek, *Phys. Plasmas* **5**, 196 (1998).
- ¹⁷A. Punjabi, A. Verma, and A. Boozer, *Phys. Rev. Lett.* **69**, 3322 (1992).
- ¹⁸A. Punjabi, H. Ali, and A. Boozer, *Phys. Plasmas* **4**, 337 (1997).
- ¹⁹S. S. Abdullaev, K. H. Finken, and K. H. Spatschek, *Phys. Plasmas* **6**, 153 (1999).
- ²⁰I. L. Caldas, J. M. Pereira, K. Ullmann, and R. L. Viana, *Chaos, Solitons Fractals* **7**, 991 (1996).
- ²¹K. Ullmann and I. L. Caldas, *Chaos, Solitons Fractals* **11**, 2129 (2000).
- ²²E. C. da Silva, I. L. Caldas, and R. L. Viana, *IEEE Trans. Plasma Sci.* **29**, 617 (2001).

- ²³E. C. da Silva, I. L. Caldas, and R. L. Viana, *Phys. Plasmas* **8**, 2855 (2001).
- ²⁴E. C. da Silva, I. L. Caldas, and R. L. Viana, *Chaos, Solitons Fractals* **14**, 403 (2002).
- ²⁵R. L. Viana and D. B. Vasconcelos, *Dyn. Stab. Syst.* **12**, 75 (1997).
- ²⁶S. S. Abdullaev, Th. Eich, and K. H. Finken, *Phys. Plasmas* **8**, 2739 (2001).
- ²⁷S. Bleher, C. Grebogi, E. Ott, and R. Brown, *Phys. Rev. A* **38**, 930 (1988); S. Bleher, C. Grebogi, and E. Ott, *Physica D* **46**, 87 (1990).
- ²⁸C. Grebogi, E. Ott, and J. A. Yorke, *Physica D* **7**, 181 (1983).
- ²⁹A. Péntek, T. Tél, and Z. Toroczkai, *J. Phys. A* **28**, 2191 (1995).
- ³⁰H. Varvoglis, K. Katsonis, M. Savopoulos, and G. Maynard, *Phys. Scr.* **62**, 1 (2001).
- ³¹Z. Kovács and L. Wiesenfeld, *Phys. Rev. E* **51**, 5476 (1995).
- ³²J. Aguirre, J. C. Vallejo, and M. A. F. Sanjuan, *Phys. Rev. E* **64**, 066208 (2001).
- ³³Z. Toroczkai, G. Károlyi, A. Péntek, T. Tél, and C. Grebogi, *Phys. Rev. Lett.* **80**, 500 (1998).
- ³⁴M. Y. Kucinski and I. L. Caldas, *Z. Naturforsch., A: Phys. Sci.* **42**, 1124 (1987).
- ³⁵M. Y. Kucinski, I. L. Caldas, L. H. A. Monteiro, and V. Okano, *J. Plasma Phys.* **14**, 303 (1990).
- ³⁶P. M. Morse and H. Feshbach, *Methods of Theoretical Physics* (McGraw Hill, New York, 1953), Vol. 2.
- ³⁷A. Vannucci, I. C. Nascimento, and I. L. Caldas, *Plasma Phys. Controlled Fusion* **31**, 147 (1989).
- ³⁸R. L. Viana, *Chaos, Solitons Fractals* **11**, 765 (2000).
- ³⁹S. S. Abdullaev, *J. Phys. A* **32**, 2745 (1999).
- ⁴⁰E. C. da Silva, I. L. Caldas, and R. L. Viana, *Braz. J. Phys.* **32**, 39 (2002).
- ⁴¹A. J. Lichtenberg and M. A. Lieberman, *Regular and Chaotic Dynamics*, 2nd ed. (Springer-Verlag, New York, 1992).
- ⁴²S. W. McDonald, C. Grebogi, E. Ott, and J. A. Yorke, *Physica D* **17**, 125 (1985).
- ⁴³S. W. McDonald, C. Grebogi, E. Ott, and J. A. Yorke, *Phys. Lett. A* **99**, 415 (1983).
- ⁴⁴Z. You, E. J. Kostelich, and J. A. Yorke, *Int. J. Bifurcation Chaos Appl. Sci. Eng.* **1**, 605 (1991).
- ⁴⁵H. Kantz and P. Grassberger, *Physica D* **17**, 75 (1985).
- ⁴⁶L. Poon, J. Campos, E. Ott, and C. Grebogi, *Int. J. Bifurcation Chaos Appl. Sci. Eng.* **6**, 251 (1996).
- ⁴⁷G.-H. Hsu, E. Ott, and C. Grebogi, *Phys. Lett. A* **127**, 199 (1988).
- ⁴⁸Z. Toroczkai, G. Károlyi, Á. Péntek, T. Tél, C. Grebogi, and J. A. Yorke, *Physica A* **239**, 235 (1997).
- ⁴⁹C. Grebogi, E. Ott, and J. A. Yorke, *Phys. Rev. Lett.* **56**, 1011 (1986).
- ⁵⁰A. Péntek, Z. Toroczkai, T. Tél, C. Grebogi, and J. A. Yorke, *Phys. Rev. E* **51**, 4076 (1995).
- ⁵¹H. E. Nusse and J. A. Yorke, *Science* **271**, 1 (1996).
- ⁵²J. Kennedy and J. A. Yorke, *Physica D* **51**, 213 (1991).
- ⁵³H. E. Nusse and J. A. Yorke, *Physica D* **90**, 242 (1996).